Can. J. Remote Sensing, Vol. 28, No. 6, pp. 794–813, 2002

An airborne synthetic aperture radar (SAR) experiment to support RADARSAT-2 ground moving target indication (GMTI)

C.E. Livingstone, I. Sikaneta, C.H. Gierull, S. Chiu, A. Beaudoin, J. Campbell, J. Beaudoin, S. Gong, and T.A. Knight

Abstract. As part of the preparatory work for the RADARSAT-2 moving object detection experiment (MODEX special operating mode), an airborne experiment was conducted at Canadian Forces Base Petawawa in July 1999 to study synthetic aperture radar (SAR) along-track interferometry (ATI) and SAR displaced phase centre antenna (DPCA) as candidate measurement techniques. The CV 580 SAR system operated by Environment Canada was configured as a two-aperture temporal interferometer, and data were collected over an experiment site that contained coordinated, global positioning system (GPS) monitored, moving targets. A robust ATI phase probability density function was identified and used in conjunction with a moving-target matched filter to extract and measure target motion. Corner reflector and vehicle velocities were measured for target speeds between 9 and 100 km/h to within 5% accuracy. SAR ATI and SAR DPCA performed equally well over this range of velocities, but ATI appears to be the more robust processing algorithm.

Résumé. Dans le cadre de la phase préparatoire à l'expérience MODEX (moving object detection experiment, MODEX special operating mode) associée à RADARSAT-2, une expérience aéroportée a été réalisée à la Base canadienne de Petawawa, en juillet 1999, pour étudier le potentiel de l'interférométrie longitudinale RSO (ATI, along-track interferometry) et de la technique RSO de déplacement de phase de centre d'antenne (DPCA, displaced phase centre antenna) en tant que techniques de mesure privilégiés. Le système RSO CV 580 exploité par Environnement Canada a été configuré comme un interféromètre temporel à deux ouvertures et les données ont été acquises au-dessus d'un site expérimental contenant des cibles mobiles coordonnées et repérées par GPS. Une fonction robuste de densité de probabilité de phase ATI a été identifiée et utilisée en conjonction avec un filtre adapté aux cibles mobiles pour extraire et mesurer le mouvement de la cible. Un réflecteur trièdre et des vitesses des véhicules ont été mesurés pour des vitesses variant de 9 à 100 km/h avec une précision de 5% près. L'interférométrie longitudinale RSO et la technique DPCA RSO ont enregistré des performances semblables à travers l'ensemble des vitesses, mais l'interférométrie longitudinale semble constituer l'algorithme de traitement le plus robuste.
[Traduit par la Rédaction]

Introduction

The RADARSAT-2 moving object detection experiment (MODEX) will provide the first opportunity to routinely measure and monitor vehicles moving on the Earth's surface from space. In historical terms this is a ground moving target indication (GMTI) mode. The RADARSAT-2 synthetic aperture radar (SAR) antenna design allows the antenna to be partitioned into two halves along the direction of flight and thus permits two closely spaced observations to be made of the same scene to observe temporal changes (Meisl et al., 2000). As the radar system is fundamentally a strip-mapping SAR, the total observation time for any point on the Earth's surface is limited to the time that the radar beam illuminates the point as it sweeps by. The dwell time for velocity measurements cannot exceed the real aperture time of the radar. Object motion is measured using the SAR moving target indication (MTI) techniques: along-track interferometry (SAR ATI), or displaced phase centre antenna (SAR DPCA) (Thompson and Livingstone, 2000).

The RADARSAT-2 MODEX capability is being built into the satellite system by the developer, MacDonald Dettwiler and Associates, with collaboration and sponsorship by the Canadian Space Agency (CSA) and the Canadian Department of National Defence (DND). The DND RADARSAT-2 GMTI Demonstration Project provided initial specifications for the MODEX mode of operation, is collaborating on its development, and is developing the ground processing and information extraction infrastructure needed to conduct GMTI investigations. One of the key objectives of the DND GMTI project is to assess the strengths and weaknesses of space-based

Received 18 May 2001. Accepted 9 July 2002.

C.E. Livingstone, I. Sikaneta,[1] C.H. Gierull, S. Chiu, A. Beaudoin, J. Campbell, and J. Beaudoin. Defence Research Establishment Ottawa, 3701 Carling Avenue, Ottawa, ON K1A 0Z4, Canada.

S. Gong and T.A. Knight. MacDonald Dettwiler and Associates, 13800 Commerce Parkway, Richmond, BC V6V 2J3, Canada.

[1]Corresponding author (e-mail: ishuwa.sikaneta@drdc-rddc.gc.ca).

SAR GMTI systems for measuring cultural activities on the Earth's surface.

The development of the ground processing – analysis infrastructure for RADARSAT-2 MODEX will be based on models derived from theoretical understanding of the measurement process. These models are validated by airborne SAR GMTI experiments and by simulation (Chiu et al., 2000) of the spacecraft radar performance and observation geometries. The experimental airborne GMTI measurements used the two-aperture ATI mode of the CV 580 SAR system (Livingstone et al., 1995) operated by Environment Canada to provide experimental data for RADARSAT-2 resolution and incidence angles. A space-based radar GMTI simulator SBRMTISIM, developed by Sicom Systems Ltd., was used to test the extrapolation of airborne measurements and results to the RADARSAT-2 operating parameters and observation geometry (Chiu et al., 2000; Chiu and Livingstone, 2002).

This paper describes the results obtained from an airborne ATI experiment conducted at Canadian Forces Base Petawawa in July 1999.

Background

SAR images of moving targets

The formation of a SAR image relies on an accurate model of the imaging system, the transmitted signal, the imaging geometry, the terrain surface, and its evolution through time. Relative motion between the radar platform and the target is a key element in such a model. Further details of the image-formation processes and algorithms are discussed elsewhere (Franceschetti and Lanari, 1999) for moving targets.

A conventional range–azimuth coordinate system is assumed in which the azimuth direction on the imaged surface is taken to be parallel to the motion of the radar. Assuming range compression, the imaging geometry model for any target point (x, y, z) on the imaged surface can be expressed in terms of the systematic phase history. If the radar position is given by $\vec{R}_P(t) = [x_P(t), y_P(t), z_P(t)]$, the target position is given by $\vec{R}_T(t) = [x_T(t), y_T(t), z_T(t)]$, and time t is defined as zero when the radar is broadside to the target, then the relative systematic phase history $\theta(t)$ is given by

$$\theta(t) = \frac{4\pi}{\lambda}(|\vec{R}(t)| - |\vec{R}(0)|), \quad t \in \left[-\frac{T}{2}, \frac{T}{2}\right], \tag{1}$$

where the range $\vec{R}(t) = \vec{R}_P(t) - \vec{R}_T(t)$, and λ is the radar wavelength. For a SAR operation, the duration, T, is the maximum usable synthetic aperture time. $\theta(t)$ defines the matched filter needed to focus SAR data along a hyperbola to form an image from the range-compressed and sampled signal time history. Commonly, $\vec{R}_T(t) = \vec{R}_T$ (the target position has no time dependence), and $\theta(t)$ defines a stationary-world matched filter (SWMF). The quality and focus of the resulting image are constrained by noise and noise-like processes and the knowledge of the relative motion of the radar and target together with the fidelity of the processor in applying the matched filter. Such processes may include the additive noise of the radar, the radar phase noise, and multiplicative noise components caused by data measurement and sampling limitations.

If the time dependence of $\vec{R}_T(t)$ is ignored, SWMF may poorly represent the phase history of a moving object. The radar returns from poorly matched objects can be distributed over many resolution cells in images produced under the stationary-world assumptions. They will generally be displaced in azimuth from their proper image position and will be superimposed on correctly positioned radar returns from unrelated terrain. Signals from badly mismatched objects may not be discernible at all easily in the SAR image.

The image-domain representation of mismatched moving targets will be dominated by four effects: range walk, azimuth impulse response broadening, azimuth smearing, and azimuth displacement. Depending on the characteristics of target motion, any combination of these four effects may be apparent (Raney, 1971; Freeman, 1984; Ender, 1996).

Range walk

For radar range resolution, ρ_R, the target range walk D for a particular point target can be expressed in range cells as

$$D = \frac{\max\{|\vec{R}(t)|\} - \min\{|\vec{R}(t)|\}}{\rho_R}, \quad t \in \left[-\frac{T}{2}, \frac{T}{2}\right]. \tag{2}$$

When $D > 1$, significant range walk has occurred and the target signal (signal energy) will be distributed over two or more range cells. If the range cell migration of signal energy is not compensated during the SAR processing, only part of the target history will be represented in each cell and the azimuth impulse response width of the target will broaden.

Azimuth impulse response broadening

The target signal distribution in range will contribute to the azimuth impulse broadening effect by reducing the effective matched-filter length for each target range cell. This effect is caused by both the imaging geometry (traditional range migration) and an additional component due to the target motion.

When the radial target speed, $s = \frac{d\vec{R}_T(t)}{dt}\frac{\vec{R}}{|\vec{R}|}$, is nearly constant over aperture time T, the target motion yields an effective azimuth matched-filter length (bandwidth) reduction factor, α, and an azimuth impulse response width broadening factor, f, for each target range cell that is fully spanned by target signal data:

$$\alpha = \frac{1}{\frac{sT}{\rho_R} + 1}, \quad f = \frac{sT}{\rho_R} + 1. \tag{3}$$

Target motion in the direction of travel of the radar also induces an azimuth impulse response width broadening effect. In such a situation, the phase history of a moving target will be either compressed or stretched in time. For a transformation such as $\theta(t) \rightarrow \theta(kt)$, an imaged target will be smeared into $N_a|(1 - 1/k)|$ extra cells, where N_a is the number of azimuth cells that span the beam width, and k is the time compression factor.

Azimuth displacement

The filter for the moving target and the terrain is mismatched when the range time for the radial component of the target velocity is a significant fraction (>1%) of the square of the radar velocity. An uncompensated target radial velocity will result in a target azimuth shift in the image plane. In the SAR process, an object with non-zero mean radial velocity, over aperture time T, is displaced in azimuth by a distance equivalent to the spatial shift, d, equivalent to imaging stationary terrain at an azimuth squint angle such that the terrain has the same mean radial velocity as the target. Equating the target Doppler shift at the beam centre to the stationary-world Doppler shift at squint angle β yields the displacement

$$d = \left. \frac{\left\{ \frac{d\vec{R}_T(t)}{dt} \right\} \vec{R}(t)}{\left| \frac{d\vec{R}_P(t)}{dt} \right|} \right|_{t=0} \tag{4}$$

The result of processing a moving object by using a matched filter defined for a stationary object is a displacement and smearing of the target energy in the resulting image. Conversely, if the image-formation process uses a focusing filter matched to the moving target, the target is then well focused and in the correct image coordinate location, whereas the stationary scene is distorted and displaced. Starting from a stationary-scene assumption (no prior target knowledge), the challenge is to detect moving targets, estimate their velocity, and then focus and insert them into the correctly imaged terrain.

SAR measurement of target motion

The measurement of object motion using SAR requires two operations. These operations are the detection of the movers in the SAR data, and the estimation of their velocity vectors in the slant-range plane. Target detection and velocity estimation can be performed either incoherently, with a single SAR aperture, or coherently, with two or more apertures (Ender, 1996; 1999; Barbarossa, 1992).

Once a mover is located, the range walk, azimuth displacement, azimuth smear, and defocusing effects all provide noncoherent clues to target motion in SAR data. Single-aperture techniques can be used to provide a coarse estimation of target velocity for sufficiently strong, sufficiently fast targets. Successful velocity estimation will be contingent upon reliable separation of target size effects and motion spreading effects.

If the SAR signal spectrum is filtered into overlapping sub-bands in the azimuth direction, each sub-band will then correspond to a subdivision of the radar's azimuth illumination beam into overlapping sub-beams. When each sub-beam data set is focused to a SAR image, each of the images will have observed the same scene elements at different times. Features whose range location has shifted from one sub-beam scene to the next are moving-target candidates. The shift divided by the difference in observation time provides a first, rough estimate of radial velocity.

Moving-target candidates that are not visible in a SAR image processed with an SWMF can be found by processing the scene data set for several hypothetical radial velocities that are selected to be in a "reasonable" range. Image features that become more prominent at non-zero hypothetical speeds are identified for further investigation. A combination of sub-beam centroid shift and target enhancement as a function of matched-filter velocity hypothesis provides a refined radial velocity estimate (this approach was originally used in SAR processing of airborne data to compensate for poor aircraft velocity data (Livingstone et al., 1995)). Successive processing iterations of candidate target subscenes varying range walk compensation and range and azimuth target velocity hypotheses can be used to provide a target velocity estimate in the slant-range plane of the radar. The sensitivity of this noncoherent approach and the resulting accuracy of the inferred target velocities are dependent on the fundamental resolution of the radar mode used to generate the images.

If the radar antenna is partitioned into two or more apertures that are distributed along the direction of motion of the radar, and if the design allows each aperture to be assigned to a separate, physical receiver channel, then coherent processing of simultaneously received signals can be used to find moving targets and estimate their velocities. The fundamental principle of this process is that each aperture (phase centre) observes the scene from the same point in space at a different time. In consideration of sampling ambiguity effects, the azimuth sampling of the radar (pulse repetition frequency) must be increased to adequately sample each aperture.

Partition of the antenna into two apertures results in each aperture having a larger azimuth beam width than the combined antenna. The synthetic aperture time, T, will increase and thus the observation time available for the incoherent (impulse response based) estimation processes discussed previously will increase. For an aperture phase centre separation of distance L, the time lapse between terrain observations from the same point in space is

$$\tau = \frac{L}{|\vec{v}_{radar}|}, \tag{5}$$

where $\tau << T$, and $\vec{v}_{radar}$ is the radar velocity. Typically, τ has values between one half and a few milliseconds for the CV 580 system. When relatively calibrated SAR data from each aperture are focused to a complex image (using the same

matched filter for each image) and then spatially registered to each other, the image content will be common except for scene changes over time τ. For land (as opposed to ocean) scenes, "fixed" elements are stationary over time τ and their image representations will be very nearly identical. Moving objects, however, will be displaced between the two scenes, and these displacements can be measured to fractional wavelength accuracies as phase shifts.

Two different analytical approaches can be used to find and measure moving targets: temporal (along-track) SAR interferometry (SAR ATI), and SAR displaced phase centre antenna (SAR DPCA).

SAR along-track interferometry

SAR ATI analysis exploits the correlation between the complex sample sets of the first aperture image, S_1, and the second aperture image, S_2, to produce the interferogram matrix

$$I = S_1 S_2^* = |S_1||S_2| \exp[j(\varphi_1 - \varphi_2)], \quad (6)$$

where φ_1 and φ_2 are the phase angles of the first and second aperture images, respectively, and j is the imaginary unit.

When I is plotted point by point on the complex plane, the phase difference between the source images appears as an angle measured from the positive real axis, and the amplitude (power) appears as distance from the origin. Stationary points map into a cluster about the real axis and, in the absence of target acceleration, sufficiently strong moving targets appear along their phase radial as shown schematically in **Figure 1**. The interferogram phase angles $\psi = \varphi_1 - \varphi_2$ can be related to the radial speed, s_{targ}, of the scene elements by

$$s_{\text{targ}} = \frac{\psi \lambda}{4\pi\tau}, \quad (7)$$

where λ is the radar wavelength. At $\psi = \pi \pm \varepsilon$, the scene element direction (towards or away from the radar) becomes ambiguous. This ambiguity can be resolved by sub-beam partitioning as discussed previously.

For an ideal, "noise-free" radar and rigorously stationary scatterers, stationary interferometer scene elements would be completely coherent and would map to the real axis. Partial decorrelation of the radar signals over the SAR aperture time results in the measured points being clustered in the vicinity of the real axis. Decorrelation mechanisms include additive noise in the radar system, the phase noise of the radar, and motion of clutter over the observation period. In the complex plane map of the interferogram, additive noise will appear as a point distribution about the positive real axis and the root mean square (RMS) width of the distribution will be independent of signal strength. Phase noise will appear as a distribution about the positive real axis whose RMS width limits to a constant phase angle for large-amplitude signals. The distribution created by clutter motion will have amplitude-dependent RMS width properties whose details will depend on the strength of the contribution of the moving elements to the radar scene. Fine registration errors between the two images appear as a systematic phase function that varies slowly over the interferogram and must be removed.

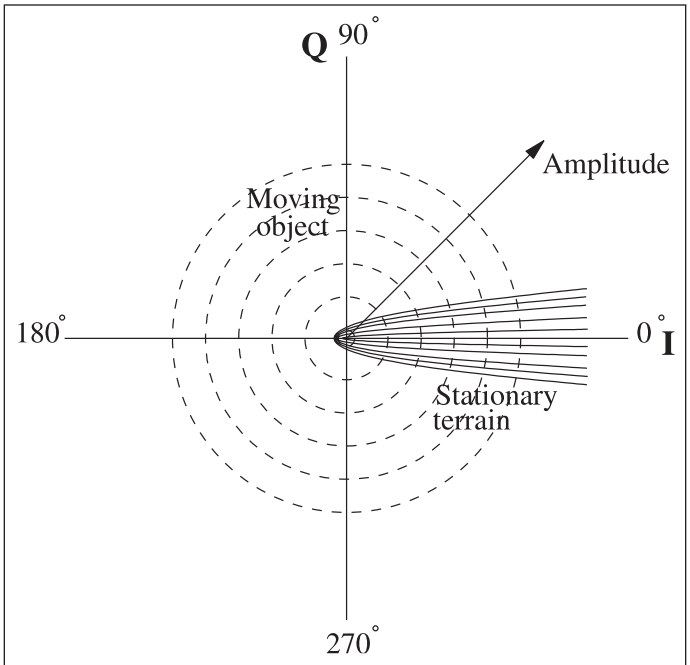

Figure 1. Schematic diagram of the ATI complex plane. Except for thermal noise near the origin, stationary terrain returns map into a statistical distribution about the positive real axis. Radar returns from moving objects with the same radial velocity appear along constant phase radials. The three target points shown in this drawing represent three samples of the same moving object. I, in phase component; Q, quadrature component.

The statistics of the intensity and phase of multichannel SAR imagery have been studied for the purpose of extracting and using polarimetric information in the detection and discrimination of targets signatures in ground clutter background (Joughin et al., 1994; Novak et al., 1989; Touzi and Lopes, 1996). For across-track (spatial) SAR interferometry, knowledge of image-pair statistics is crucial to quantitatively analyse the influence of decorrelation on the phase statistics and hence on the achievable height accuracy (Lee et al., 1994; Just and Bamler, 1994).

These statistics are, in principle, directly applicable to the problem of moving-target detection via along-track interferometry (Gierull, 2001). All published derivations use the underlying assumption of jointly Gaussian-distributed data in the two images. This requires very rough surfaces (on the scale of the wavelength) that are regionally homogeneous (statistically). The amplitude of the backscattered signal corresponds to a constant, mean radar cross section (RCS) across each region. The resulting complex image may be regarded as the sum of statistically independent contributions from many elementary scattering areas and has complex, normal distribution functions.

The jointly Gaussian assumption has been validated in most agricultural and heavily vegetated areas but has not been established for heterogeneous regions such as urban areas. Among many non-Gaussian statistics studied, the *K* distribution has proven to be useful in characterizing the amplitude distribution of electromagnetic echoes from heterogeneous terrain and from the sea surface (Yueh and Kong, 1989). The *K* distribution results when the mean RCS of the individual scatterer is itself randomly distributed with a chi-square distribution on spatial scales close to or larger than the spatial resolution (Joughin et al., 1994). The statistics of the phase and magnitude of the interferogram for general, non-Gaussian image distributions cannot be modelled analytically.

To reduce the speckle, polarimetric and interferometric data are frequently multi-look processed. Multi-look interferometric processing requires averaging several independent one-look interferograms.

The complex multi-look interferogram, Equation (6), can be rewritten as

$$I = S_1 S_2 = |I| \exp(j\psi) = \sqrt{E[|S_1|^2]E[|S_2|^2]}\ \eta \exp(j\psi), \quad (8)$$

where η is the interferogram magnitude normalized to the preceding square-root function in which $E[]$ is the expectation operator. Under the Gaussian assumptions, the joint probability $p(\eta, \psi)$ of the phase and the normalized multi-look magnitude of the interferogram is given by

$$p(\eta, \psi) = \frac{2n^{n+1}\eta^n}{\pi\Gamma(n)(1-|\rho|^2)} \exp\left(\frac{2n\eta|\rho|\cos(\psi)}{1-|\rho|^2}\right) \times K_{n-1}\left(\frac{2n\eta}{1-|\rho|^2}\right), \quad (9)$$

where n is the number of looks, $\Gamma(n)$ is the gamma function, $K()$ is the modified Bessel function (Lee et al., 1994; Joughin et al., 1994; Touzi et al., 1999), and $|\rho|$ is the magnitude of the complex correlation coefficient ρ of the images S_1 and S_2:

$$\rho = \frac{E[S_1 S_2^*]}{\sqrt{E[|S_1|^2\ E[|S_2|^2]}} \quad (10)$$

An example of the function $p(\eta, \psi)$ is plotted in **Figure 2**. It illustrates typical phase probability density function (PDF) behaviour in that large phase fluctuations are associated with small, normalized, clutter amplitudes, and the phase variations are drastically reduced for large radar returns.

Integrating Equation (9) over either of the variables leads to the marginal multi-look density functions for the normalized magnitude:

$$p(\eta) = \frac{4n^{n+1}\eta^n}{\Gamma(n)(1-|\rho|^2)} I_0\left(\frac{2n\eta|\rho|}{1-|\rho|^2}\right) K_{n-1}\left(\frac{2n\eta}{1-|\rho|^2}\right), \quad (11)$$

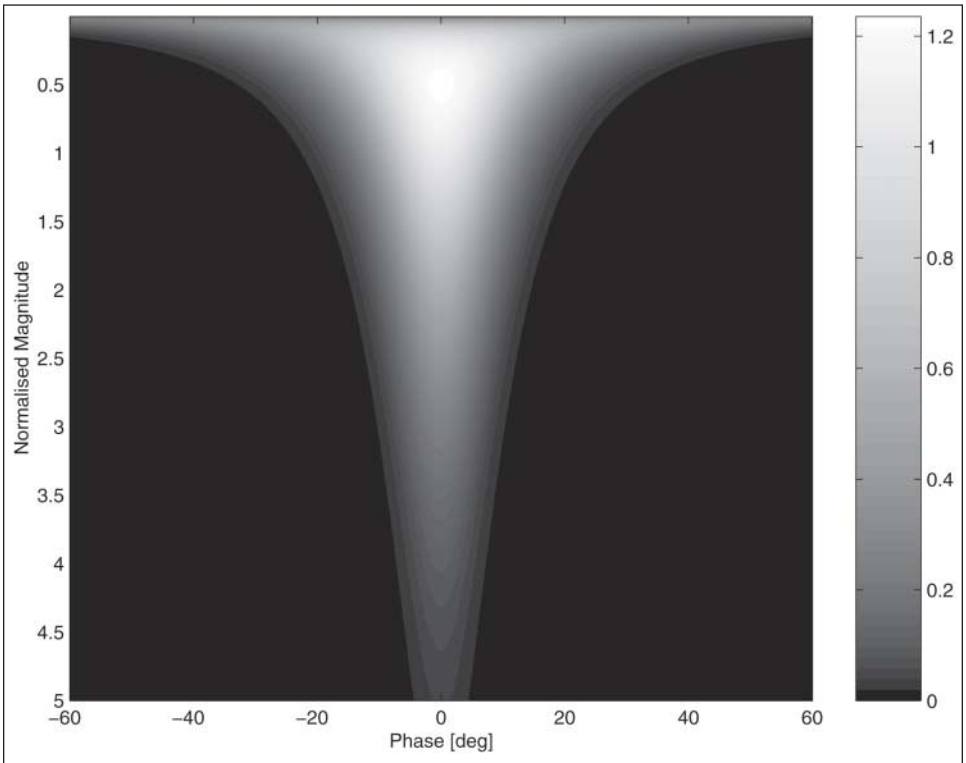

Figure 2. Theoretical joint probability density function of the one-look interferometric phase and normalized magnitude. The coherence between the single images is $|\rho| = 0.981$.

where $I_0()$ denotes the Bessel function of the first kind, and the phase in terms of the Gauss hypergeometric function ${}_2F_1()$

$$p(\psi) = \frac{\Gamma(n+1/2)(1-|\rho|^2)^n\beta}{2\sqrt{\pi}\Gamma(n)(1-\beta^2)^{n+1/2}} + \frac{(1-|\rho|^2)^n}{2\pi}.$$

$${}_2F_1(n,1;1/2;\beta^2), \quad -\pi < \psi \le \pi \tag{12}$$

where $\beta = |\rho|\cos(\psi)$ (Lee et al., 1994; Joughin et al., 1994). A comparison of these theoretical results with experimental data is given in a following section.

The marginal phase and amplitude distributions can be used to estimate the probability that a given complex data sample belongs to the stationary world. If, for instance, the size of the moving target is on the order of the spatial resolution, one possible test statistic is a comparison of the phase of the cell with a threshold derived from the marginal phase distribution. This assumption means that the backscatter power contained in the cell is dominated by returns from the desired target and that the clutter contributions to the signal are negligible. The threshold can be determined as the α-fractile of the probability density function in Equation (12), where α denotes a given false alarm rate. In cases where the spatial resolution is much larger than the target size, the clutter power can no longer be neglected. Here, the "clutter only" hypothesis has to be tested against the alternative "clutter plus target". The maximum likelihood quotient criterion could be used to derive test statistics (Novak et al., 1989).

A detection threshold function can be defined to automatically extract all moving targets that are adequately focused by the current SAR processing assumption. Under the detection hypothesis, all ATI complex plane points that lie outside of the stationary-world detection envelope are identified as moving objects. Targets that move with constant velocity over the SAR aperture time will be clustered in a narrow range of phase angles and can be assigned radial speed by phase measurement. Reprocessing data with several different target motion hypotheses and applying ATI to the resulting images can be used to detect and measure the properties of targets that have been masked by incorrect SAR processing assumptions. The radial speed hypothesis that yields the best target focus will usually resolve directional ambiguities for the airborne SAR case considered here.

SAR displaced phase centre analysis

SAR DPCA analysis starts from the same registered, complex images used for ATI. In this process the two images are subtracted to yield

$$J = S_1 - S_2 = |S_1|(e^{j\varphi_1} - e^{j\varphi_2})$$

$$= 2|S_1|\sin\frac{\varphi_1-\varphi_2}{2}\, e^{j\left(\frac{\varphi_1+\varphi_2}{2}+\frac{\pi}{2}\right)} \tag{13}$$

The magnitude of the subtracted DPCA signals is of the form $\sin(x)$, where the argument of the sinusoidal function x is directly proportional to the radial speed s_{targ} of the scene elements:

$$|J| = 2|S_1|\left|\sin\frac{\varphi_1-\varphi_2}{2}\right| = 2|S_1|\left|\sin\left(\frac{2\pi\tau s_{\text{targ}}}{\lambda}\right)\right| \tag{14}$$

The phase, ϕ, of DPCA signals can be expressed as

$$\phi = \frac{\varphi_1+\varphi_2}{2} \pm \frac{\pi}{2} \tag{15}$$

As in the ATI case, fine registration errors between the two images will appear as a systematic, slowly varying phase function that must be removed before analysis can progress.

The effect of the DPCA subtraction is to cancel all image cells whose radar returns did not change over time τ. With an ideal, noise-free radar, image cancellation is complete for stationary terrain. For real systems, complete image suppression is principally limited by the noise floor of the radar.

When the DPCA signals are plotted on the complex plane, stationary scene elements map to a circular cluster that is symmetrically distributed about the origin (uniform phase distribution) as shown schematically in **Figure 3**.

Near the origin, the signals are dominated by a composite of additive noise, nearly coherent scene differences, and phase-

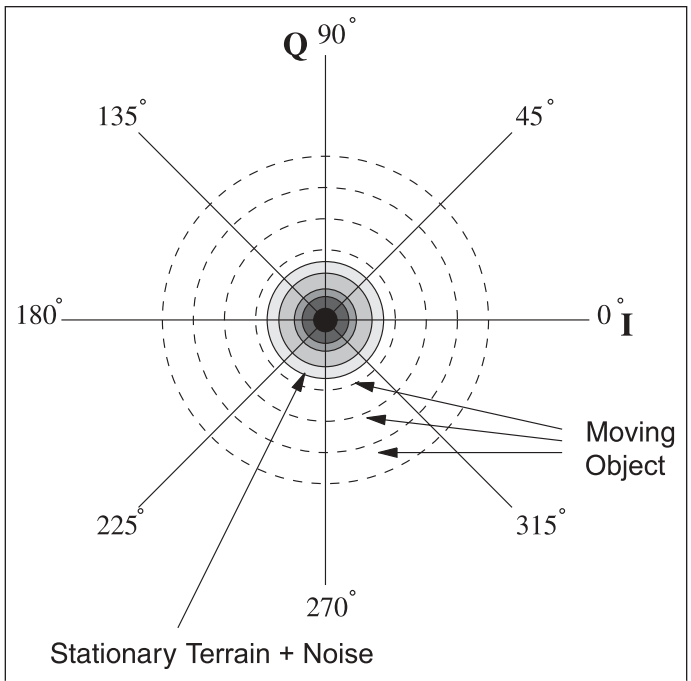

Figure 3. DPCA complex plane schematic showing target data in the vicinity of the 290° radial. Stationary terrain returns map into a symmetric distribution about the origin.

noise modulated scene elements. Moving targets appear as outlying points.

Since the DPCA magnitude of a moving target is proportional to $\sin(2\pi\tau s_{\text{targ}}/\lambda)$, the detection becomes impossible for targets with the "blind" speed $s_{\text{targ}} = (N/2)(\lambda/\tau)$, where N is an integer, as the signal magnitudes drop to zero. Maximum radar returns are achieved for targets with $s_{\text{targ}} = [(2N + 1)/4](\lambda/\tau)$.

As in the ATI case, the DPCA target signals are defocused in the image when the image-formation process model does not match the target motion. Iterative processing steps similar to those used for ATI are required to provide the best target motion estimates.

Physical size and radar cross section

For SAR GMTI measurements, the physical size of the target contributes to the target measurement process. When the resolution cell area is A and the projected (onto the slant-range plane) target area is B, with $B < A$, the terrain surface corresponding to the projection $A - B$ directly contributes signal to the target cell. Conceptually, if the terrain has a scattering coefficient, σ^0, distributed according to a probability function, P, with variance, V, and if the target has radar cross section, σ, the composite radar return measured from the resolution cell will have mean power proportional to $\sigma + (A - B)\sigma^0|_{P,V}$. The notation $|_{P,V}$ defines a single statistical realization of terrain scatterer returns over a synthetic aperture time. When $(A - B)\sigma^0$ approaches σ for a moving target, the systematic phase structure of the target signal is combined with a noise-like phase contributed by the terrain surface that shares the resolution cell at nearly equal weighting, and the target becomes inseparable from the terrain. Only when the target cross section is very much larger than the summed terrain cross section can the terrain "phase noise" be ignored.

When the projected target area is larger than the radar resolution cell area, the resolution cells in the focused target image cluster will carry phase terms that represent the local motion of the corresponding dominant scatterers on the target. The differential motion of different target components is now important and the translational velocity of the target must be inferred from the individual motions of the cells in the target cluster.

Experiment description

The results presented in this paper were acquired during an experiment conducted at Canadian Forces Base (CFB) Petawawa on 14 July 1999. SAR GMTI data were acquired by the Environment Canada CV 580 C-band SAR configured in its along-track interferometer (ATI) mode. The surface component of the experiment provided GPS-monitored, controlled moving targets and video-monitored targets of opportunity. The controlled targets include a set of unobstructed, moving corner reflectors located in a low-clutter background.

Site description

CFB Petawawa training area 2 was used as the primary experiment site. The recent photomosaic (**Figure 4**) shows two moving-target ranges situated on flat, open spaces of sparse, herbaceous and shrubby vegetation in well-drained soil. Each range contains a target transporter that was used as an experiment facility. An additional, short-range transporter system, seen at the bottom of **Figure 4**, and access roads in the training area provided additional sites for the controlled moving targets. The radar cross section was relatively low over the entire area used for controlled target measurements, and target to clutter contrasts were generally high. The Trans-Canada Highway (Highway 17), seen along the right-hand side of the image, was monitored to provide a convenient source of known targets of opportunity.

Target motion studies were conducted on the Juliet (700 m) and Delta (650 m) target transport systems (**Figure 4**), which appear in the left half of the image in the upper and lower thirds, respectively. Another 60 m target transport system (moving infantry target, MIT) used in the experiment appears near the bottom of the image.

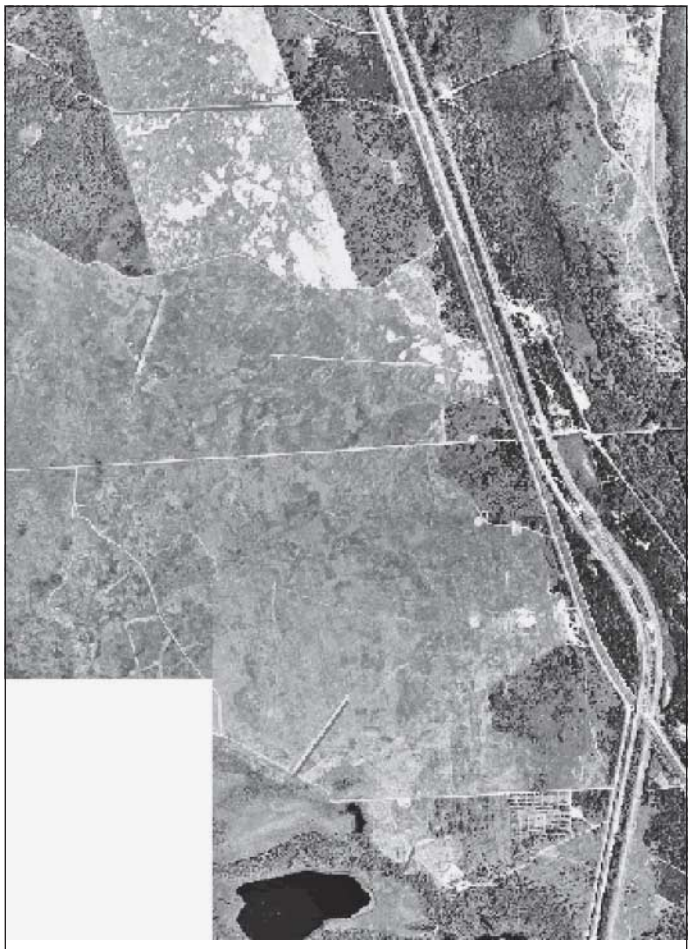

Figure 4. Aerial photograph mosaic of CFB Petawawa training areas 1 and 2.

Controlled moving targets

Five controlled ground moving targets (GMT) of differing types were used in the experiment. Target transport systems, managed by Lockheed Martin Canada, are located in the Juliet and Delta firing ranges. Two types are present, moving vehicle target (MVT) simulators (two units) and moving infantry target (MIT) simulators (one unit). These target systems consist of rail tracks and rail vehicles that can be programmed to move at predetermined speeds. Two of the dirt roads on the site provided paths for GPS-monitored truck targets (two trucks).

Each controlled moving target used in the experiment was equipped with a trihedral corner reflector and a carrier-phase, recording, GPS receiver. A stationary, carrier-phase GPS receiver was located on the site to provide a reference for differential GPS (DGPS) processing. The time histories of the differentially determined positions at 1 s intervals provided time-keyed moving-target velocity measurements that were used to validate time-keyed (the GPS clock provided the master time reference) airborne SAR measurements.

The experimental configuration of one of the two MVT targets is shown photographically in **Figure 5** and schematically in **Figure 6**. The transporter is a remotely controlled, engine-powered cart that is guided by the rail system. The MIT transporter configuration is similar to that of the MVTs but is built to a smaller scale.

The two MVTs and the MIT travelled northward during each airborne radar observation pass. The corner reflectors on GMTs were rotated by 180° between passes to face the SAR antenna boresight.

During data acquisition, the radar system observed the test area from two directions approximately corresponding to the right- and left-hand sides of **Figure 4**. Due to the brick wall, as seen in **Figures 5** and **6**, radar scattering properties differ when the MVT is illuminated from either side of the rail. Multipath contamination of the moving-target signatures was minimized by raising the corner reflector well above the wall and by orienting the radar observation geometry to eliminate specular reflections from structural elements. The MIT transporter, situated close to a forest edge, had similar features but on a smaller scale.

Two dirt roads within the site were selected for additional controlled motion experiments. The two roads are perpendicular to one another, one of them closely aligned to the flight trajectory, so significantly different radial velocities were observed by the radar for similar target ground speeds. Two pickup trucks, equipped with corner reflectors and carrier-phase GPS receivers, were directed to drive at constant speed during the SAR imaging time. Each truck drove along a predefined linear segment of road as shown in **Figure 4** and reversed its direction of travel for each of the four airborne radar passes. **Figure 7** illustrates one of the pickup trucks driving parallel to the railroad and Highway 17.

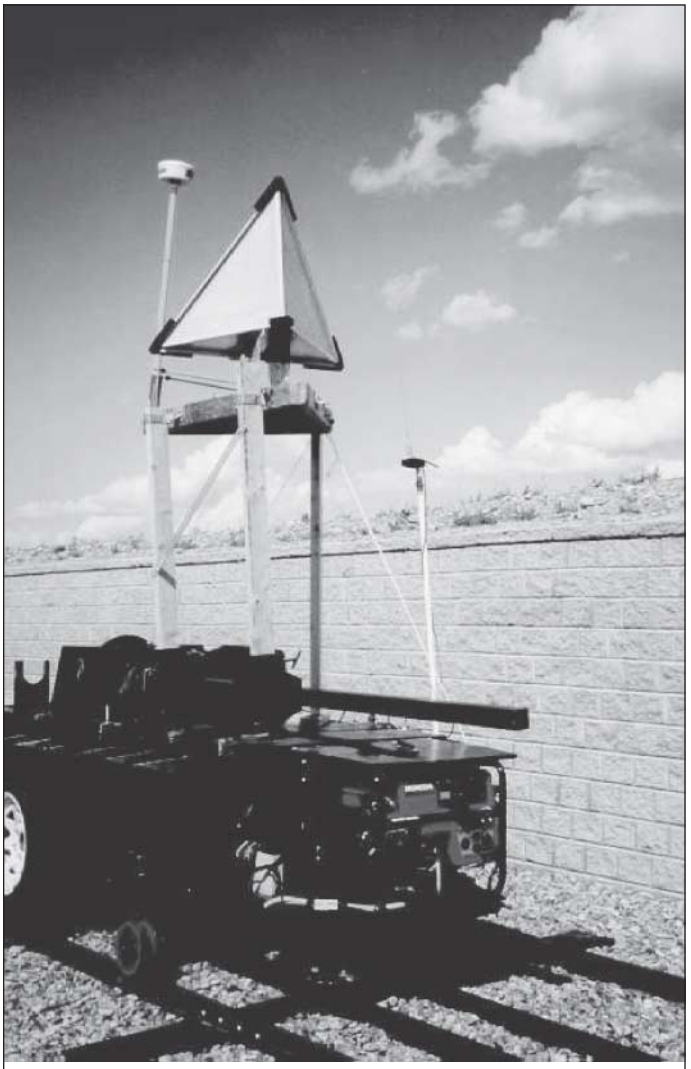

Figure 5. One of two identical MVTs on its rail, with mounted 70 cm corner reflector and DGPS antenna.

During the data-acquisition period, all controlled moving targets were synchronized with their radar observation times so

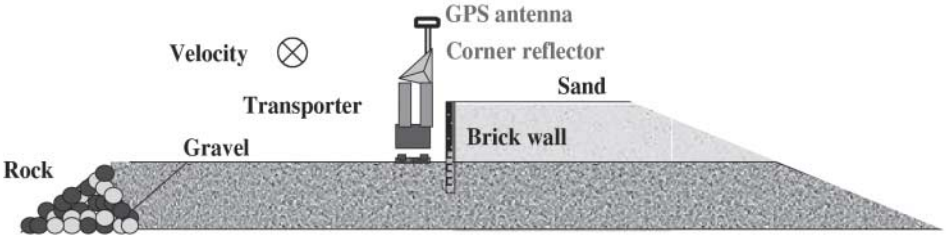

Figure 6. Cross section of MVT rail system with surrounding structure.

Figure 7. Pickup truck as a GMT on dirt road, with corner reflector and DGPS antenna.

that they were moving at nearly constant speed during the radar measurements. All corner reflectors were oriented towards the expected position of the radar when the vehicle was in the centre of the radar beam. Further details of the controlled targets are shown in **Table 1**.

Target speeds between –8.5 and +5.5 m/s were selected to provide radial velocities within the directional ambiguity speed limits. A given control speed was used at least twice for the two parallel flight lines with opposite SAR aspect angles to provide negative and positive velocity radial components.

Targets of opportunity

A 600 m straight section of Highway 17 passing through the experiment site was selected to monitor vehicles of opportunity. Two video cameras were sited along the west side of Highway 17 to record vehicle images and to provide data needed to estimate traffic speed and direction. The two cameras viewed the highway at right angles and were separated by 600 ± 0.5 m using differential GPS measurements. The cameras were set back from the roadway and were concealed by bushes to minimize driver reaction to the monitoring activity.

The two camera time-recording systems were synchronized to GPS time to within a second of each other. The video recordings of the two cameras were used to estimate the position and velocity of vehicles on the straight, short section of the highway. Since traffic volume was low and there were no obstacles or distractions near the highway test area, the constant-speed assumption used in interpreting the video data is reasonable.

Airborne component

The radar, operating at C band (5.30 GHz), was configured to use a transmitting antenna situated on the belly of the aircraft and a two-aperture (L = 0.46 m phase centre separation), microstrip receiving antenna situated on the starboard side of the aircraft above the transmit antenna. Horizontally polarized radiation was transmitted and received by the system running in the nadir mode, with most targets of interest situated at incidence angles of approximately 50°. The measured target radial speed becomes directionally ambiguous when the target displaces one-half wavelength in range over the time required for the aft antenna aperture to move to the previous position of the fore aperture. The first blind speed occurs when this displacement is one wavelength. Blind-speed values for different passes are listed in **Table 2**. To minimize azimuth ambiguity effects, the radar system was run at twice the usual pulse repetition frequency (PRF) to radar platform speed (v_{radar}) ratio (PRF/v_{radar} = 5.14 m^{-1}). Alternate pulses were recorded in separate channels and the data were interleaved for processing. At a 50° incidence angle and an altitude of approximately 7 km, targets of interest were offset from the ground projection of the radar flight track by approximately 9 km.

The ATINSAR processor, originally developed by the Canada Centre for Remote Sensing (CCRS), was enhanced to focus moving targets (Sikaneta, 2001). After azimuth compression of the fore and aft channels, the aft channel was

Table 1. Controlled ground moving targets (GMT).

GMT No. and location	Carrier and trajectory	Run length (m)	Track bearing (°; true north)	Nominal target speed (km/h)	Corner reflector side (cm)	Corner reflector RCS (m^2)
MVT-1; Juliet range	Engine-powered carrier on a level rail	700	0	20 (P7, P8); 30 (P9, P10)	85.8	706
MVT-2; Delta range	Engine-powered carrier on a level rail	650	18	10 (P7, P8); 20 (P9, P10)	69.8	309
MIT-1; No. 269	Small engine-powered carrier on a level rail	59.5	355	5	36.9	24
PU-1; Stewart Road	Pickup truck on level gravel road in open space	1000	69	50 (P7, P8); 70 (P9, P10)	76.0	434
PU-2; Messer Road	Pickup truck on level dirt road surrounded by trees	1500	323	40 (P7, P8); 60 (P9, P10)	75.9	432

Note: Track bearing angles are measured clockwise from geographic north. Target speeds were varied over the four SAR–GMTI data collection passes, P7–P10.

Table 2. SAR data set summary.

Flight No.	Flight direction (°)	Look direction (°)	Aircraft ground speed (m/s)	Target blind speed in range (m/s)	Processed segment[a]
Line 6, pass 7	118	208	124.74	15.3	20:20:36 to 20:22:36
Line 7, pass 8	298	28	127.47	15.7	20:39:11 to 20:41:10
Line 6, pass 9	118	208	129.04	15.9	20:56:59 to 20:58:59
Line 7, pass 10	298	28	131.92	16.3	21:15:00 to 21:17:00

[a]Time in hours, minutes, and seconds.

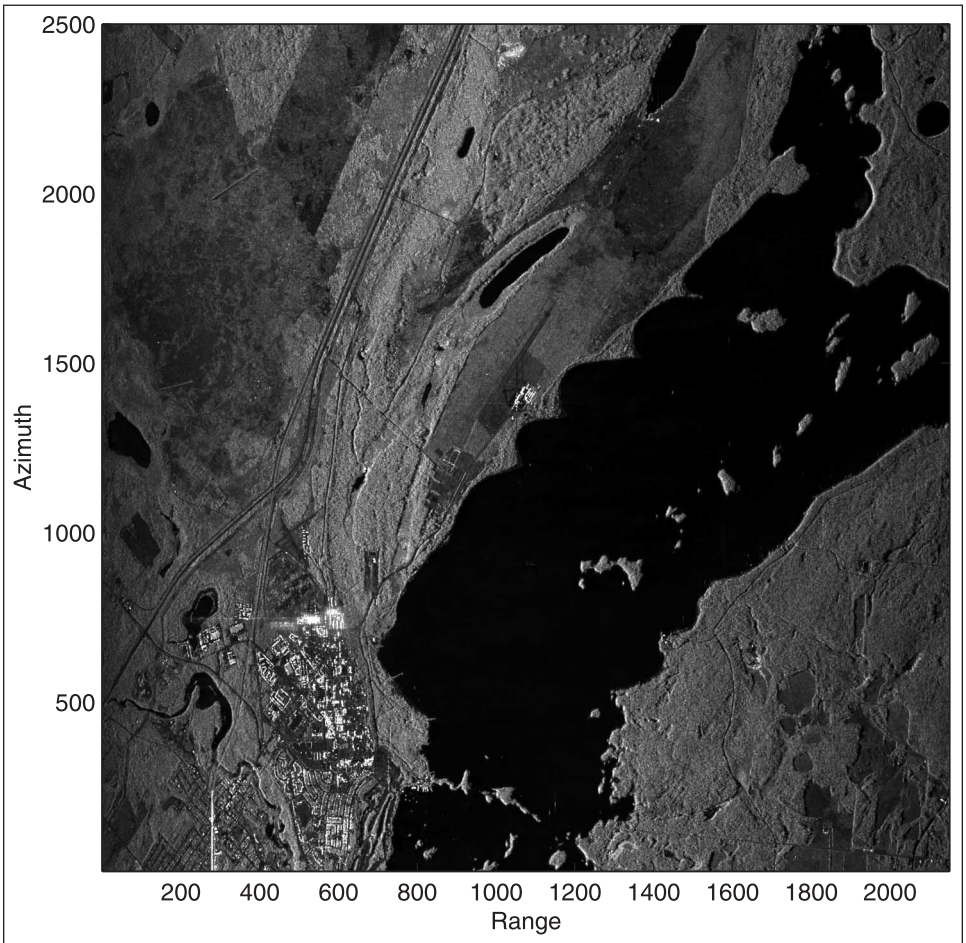

Figure 8. Horizontal transmit, horizontal receive (HH) polarized SAR image of CFB Petawawa, line 6, pass 9, 14 July 1999. The urban component of CFB Petawawa is seen at the bottom left of the image. The experiment site, including Highway 17, occupies the upper left half of the image. The left boundary of the image is parallel to the aircraft flight track (298° bottom to top).

shifted by $(L/2)(\mathrm{PRF}/v_{\mathrm{radar}})$ pixels by using an fast Fourier transform (FFT) interpolator (so that each phase centre viewed a given target from effectively the same position in space). The ATINSAR software was used for azimuth compression, image registration, and output-interferogram creation.

Systematic phase errors, resulting from local multipath effects in the antenna mount structure, were estimated from measurements on clutter data and removed by phase multiplication prior to further analysis.

Four SAR interferograms were generated from data acquired on four flight lines as summarized in **Table 2**. The resulting interferometric images form two pairs that differ in aspect angle by 180°.

Figure 8 shows how the experiment site appears as a SAR image (line 6, pass 7). CFB Petawawa is visible in the lower left portion of the image, and the Trans-Canada Highway is seen to emerge upwards from the base. The training area used for the experiment site appears as the large, low cross sectional area

above the base. The high-return area surrounding the training area is predominantly pine forest.

Results and discussion

This experiment focused on two complimentary aspects of SAR GMTI: the statistical properties of the complex signal plane for two-aperture SAR motion measurements, and SAR matched-filter adaptation for moving object measurement. The signal plane statistics provide the tools needed to separate moving objects from stationary-world radar returns. Tuning the SAR azimuth processing filter to correct for target motion allows accurate motion measurement.

The ATINSAR processor, used for this analysis, contains complex, spatial filtering and decimation functions to create a nearly square pixel geometry for display. When the radar system runs at a PRF/v_{radar} ratio of 5.14 m^{-1}, the azimuth oversampling ratio is approximately 4.5 and the range to azimuth pixel aspect ratio is approximately 20:1. The filtered data are decimated by a factor of 20 in azimuth. DPCA uses slightly different smoothing parameters than ATI to prevent oversmoothing of fore and aft channels.

ATI complex plane statistics

Figure 9 illustrates the complex plane representation of a typical SAR ATI measurement for this experiment. The upper half plane contains targets moving away from the radar, and the negative real axis defines the target direction ambiguity singularity (plane cut line). The cluster of points near the 265° radial is a moving calibration target that is not matched to the stationary-world SAR processing assumption. The small cluster of points outside of the terrain cluster near the 330° radial is a second mismatched moving target. The terrain signature scatter about the real axis is predominantly additive noise (point spread near the origin) and phase noise (the limiting angle of the point spread at large amplitudes). In this case the phase noise is bounded at one standard deviation by the $\varepsilon = \pm 2.7°$ radials. When the histogram is plotted in three dimensions (**Figure 10**) the amplitude distribution is emphasized.

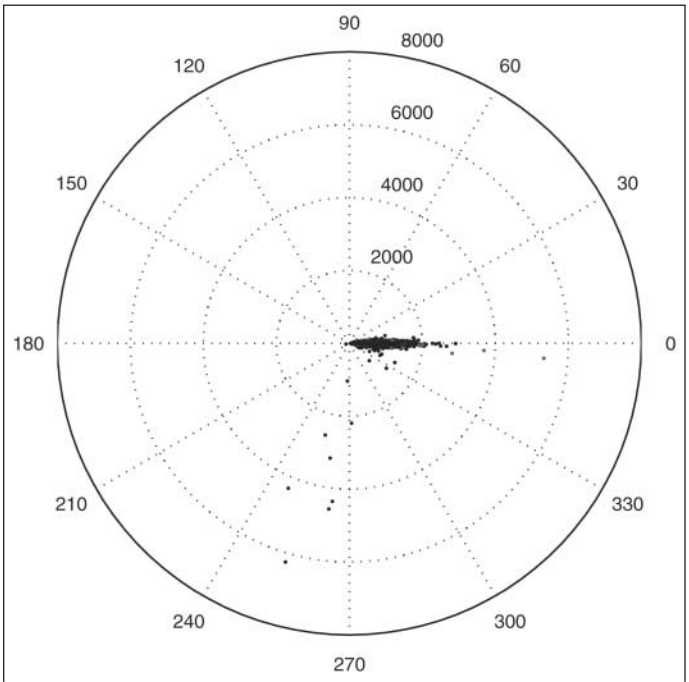

Figure 9. Land SAR ATI complex plane with two detected moving targets (line 7, pass 10, Delta range). Stationary elements are clustered about the positive real axis.

In the three-dimensional view shown in **Figure 10**, the radial direction in the horizontal (complex) plane is power, the azimuthal direction in the horizontal plane is phase angle, and the vertical axis is the number of samples. In this case there are 10^4 samples. The tail of the distribution along the negative real axis is additive noise that is uncorrelated between the two channels. The main body of the distribution is a sum of additive noise, scene content modulated by uncorrelated system phase noise, and decorrelation contributions from internal scene motion.

Several nearly homogeneous areas within line 7 of pass 10 were chosen to compare the marginal probability functions (Equations (11) and (12)) with some real clutter data. Two representative results are shown in **Figure 11**. The clutter type within patch 1 corresponds to low-scrub vegetation surrounding metal debris, and patch 24 is thickly covered with jackpines. While the phase statistics are independent of the clutter type, the magnitude statistics are not. For patch 24 the Gaussian assumption for the backscatter distribution seems to be nearly valid, whereas patch 1 shows strong disagreement. Similar magnitude and phase results have been reported from other (mainly polarimetric) studies that coherently process correlated radar channels (Lee et al., 1994; Novak et al., 1989). The results can be heuristically explained when assuming that the *K* distribution is applicable in characterizing the amplitude distribution of such ground cover. This *K* distribution can be derived by the product of a chi-square distributed random variable and the conventional Gaussian distribution of the SAR imagery (Joughin et al., 1994). It follows that, under some conditions, each single-look interferometric pixel is multiplied by the same texture random variable. As a result, the fluctuations that give rise to the amplitude *K* distribution cancel out when the phase is computed as is suggested in (Touzi et al., 1999).

The marginal phase probability density function (Equation (12)) depends only on the magnitude of the local coherence of the interferogram. For ATI, the coherence is determined by other variables, notably radar system additive noise, the composite phase noise of the scene and the radar system, and processing fidelity.

When the radar system phase noise is dominant, the coherence and the phase standard deviation are both independent of the strength of the radar returns from all terrain elements. For subscenes that contain wind-generated internal motion, both the coherence and the phase standard deviation will be influenced by scatterer motion during the aperture time.

Figure 12 illustrates the limiting phase angle effect for terrain similar to patch 1 in **Figure 11**. Here the RMS value of the quadrature component of the complex returns from patches of statistically uniform, brush-covered terrain is plotted against the signal amplitude.

The phase standard deviation can be modelled as the constant 2.4 ± 0.07° independent of signal amplitude. Pine forest areas similar to patch 24 in **Figure 11** yield a constant phase standard deviation limit of 2.98 ± 0.07°. Both results can be related to radar phase noise measurements (2.0 ± 0.2°) when wind-produced vegetation internal motion is considered. During the radar measurement period, the wind vector was within 11° of the SAR track normal at 5.2 ± 0.8 m/s. An empirical power-law model for low to moderate wind speeds (Nathanson, 1969), which estimates the RMS speed of moving vegetation components, yields an RMS internal-motion phase contribution of 1 ± 0.2° for the forest.

The dependence of the coherence, and by extension the marginal phase probability density function, on environmental conditions for some terrain cover types requires that local estimates of the scene coherence be used for the extraction of moving targets from ATI scenes.

Figure 13 shows the complex plane representation of a typical DPCA measurement for this experiment. As discussed in the section SAR displaced phase centre analysis, the central cluster of stationary object returns is statistically symmetric about the origin. The radius of this central cluster includes both additive noise and phase noise modulated by the radar returns from the stationary scene. Wind effects on vegetation broaden the distribution. Moving objects appear as points outside of the central cluster, and the magnitude of their DPCA signatures depends on both the radar cross section of the objects and their radial speed. The moving object phase angle is determined by speed alone when all systematic phase errors have been removed from the data.

In **Figure 13**, the points in the vicinity of the 85° radial are the corner reflector mounted on the Delta target transporter when a stationary-world assumption is used to define the SAR processor. The spread of the observed target points is an expected result of target defocus and cell migration caused by filter velocity mismatch.

Detection of moving targets

Range and azimuth corrections to the matched filter

As previously discussed, noncoherent techniques can provide a first estimate of the velocity of a target. A velocity-addressed matched filter can be designed to better track the characteristics of a moving target, and in turn resolve contributions from clutter that would appear if an SWMF were used to focus the SAR data. As a first approximation to the motion characteristics of a target, two constant orthogonal velocities (a ground projection of the radial velocity, or ground range velocity, and an azimuth velocity) may be used to represent the target motion. If target acceleration is also

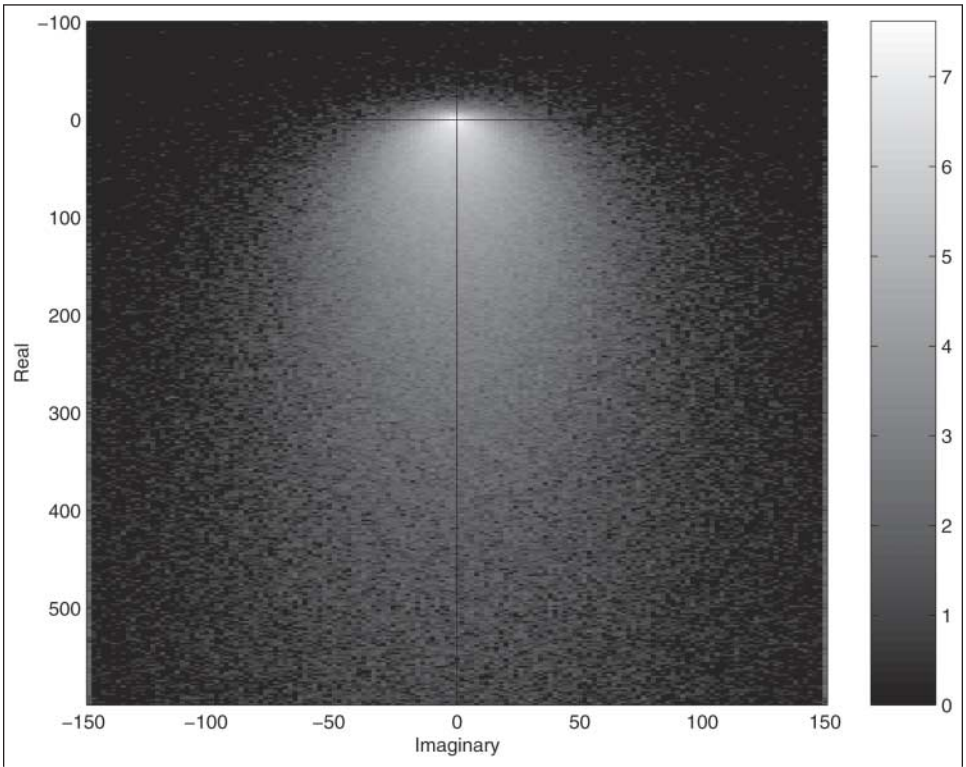

Figure 10. A three-dimensional view of a uniform terrain-cover area to illustrate the generic shape of the distributions. The distribution is oriented along the positive real axis. Two-dimensional histogram (logarithmic gray scale) of clutter (line 7, pass 10, Petawawa, 1999).

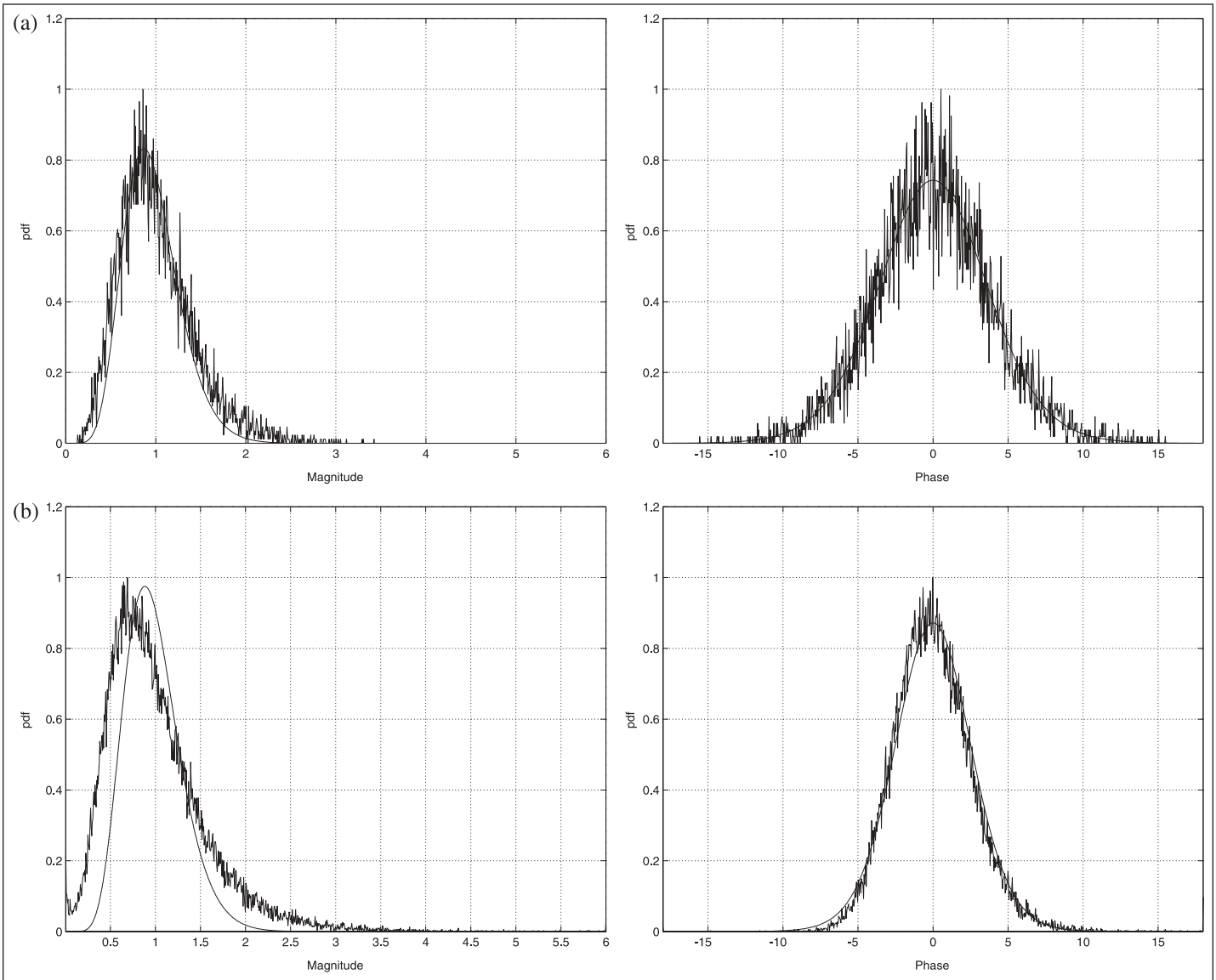

Figure 11. Comparison of the theoretical density functions and empirical histograms of the magnitudes and phases for ATI measurements on two homogeneous areas with different terrain cover: (a) patch 24, marginal PDF of magnitude, gamma = 0.965, number of looks = 10; (b) patch 1, marginal PDF of magnitude, gamma = 0.981, number of looks = 10.

suspected, two constant, orthogonal acceleration terms may be built into the model.

A velocity addressed matched filter will not only provide a first estimate of the velocity of a target, but will also complement coherent velocity estimation by gathering the energy of a target into a more cohesive, cleaner, cluster of points. Moving-target detection via ATI or DPCA techniques will be easier, and velocities estimated by using those techniques will be more accurate.

Figures 14 and **15** illustrate peaks in the response of a target versus range and azimuth velocity offsets. By reducing the azimuth impulse response width of a target, the signature of the target is more easily separated from surrounding clutter. In addition, broadening of the impulse response width for clutter reduces clutter contribution to the target. The target response is calculated as the peak power of the target. In **Figures 14** and **15**, relative target power is plotted because the data have not been radiometrically calibrated. The phase of the target has been calculated as a complex sum:

$$\theta = \arg\left(\sum_{i \in A} z_i\right) \tag{16}$$

where A defines the region within three times the 3 dB width of the target.

It is clear from **Figures 14** and **15** that the phase of the target varies with the velocity offset used for processing. The phase response is more sensitive to changes in ground range velocity than to changes in azimuth velocity. The azimuth velocity was scanned first, and then the ground range velocity was scanned by using the estimate of azimuth velocity that maximized the

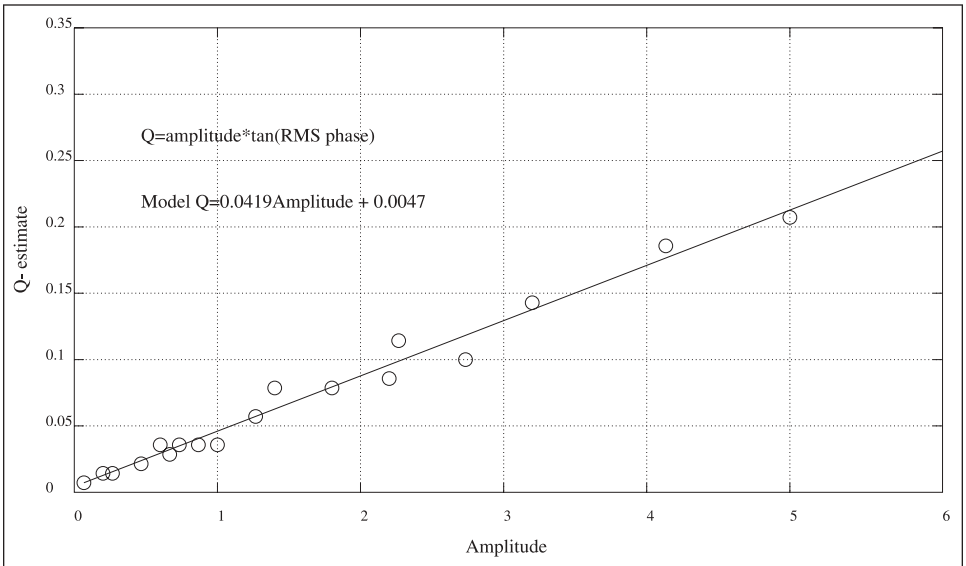

Figure 12. The limiting phase angle corresponding to phase noise dominated ATI data is the inverse tangent of the slope of the model line. The case shown is a section of an artillery training range covered by low scrub vegetation and metal debris (line 6, pass 7).

target response. The target phase estimate was extracted from the phase curve in **Figure 14** at the point where the target response was greatest.

ATI detection

Each velocity estimate (except for the small MIT target) listed in **Table 3** was calculated in exactly the same, repeatable way. Targets were first detected by nulling the amplitudes of all signal components whose phases lie within a selected threshold ("keyhole" filter). After initial detection, the noncoherent techniques described in the previous section were employed to obtain an initial velocity estimate. This, in turn, allowed velocity-adapted SAR (VASAR) processing of a window centred on the target, which minimized clutter contributions and enhanced the target. With "cleaner" representations of the moving targets, ATI techniques were then used to estimate target velocities.

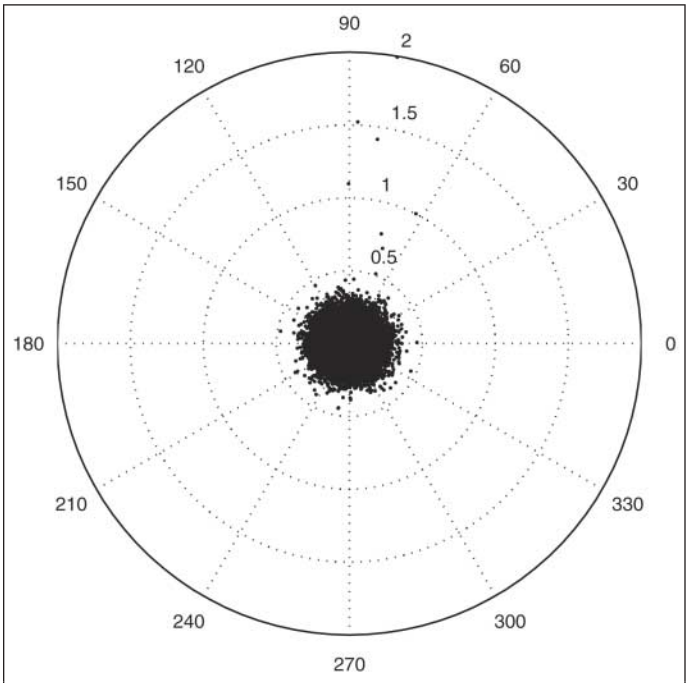

Figure 13. DPCA measurements of controlled target Delta seen in a background of low brush and stationary metal debris. The points in the vicinity of the 85° radial are target measurements prior to motion-corrected processing.

The only target not consistently detected was the slow-moving, low-RCS MIT target. The MIT was detected in two passes but was only visible when the false-alarm rate was increased by manipulating the keyhole filter parameters. In the two other passes, MIT was not detected for any filter setting. Since these detections are considered marginal, MIT velocity estimates have not been included in the results.

In two cases, the Stewart Road target was travelling at speeds and orientations that caused the SAR system to measure velocity ambiguously. This was the case for passes 7 and 8. For pass 8, the ambiguity was detected and corrected during the target matched-filtering (VASAR) process.

Results are summarized in graphical form in **Figure 16** after all corrections have been made. The composite error (ATI plus GPS) has an RMS value of 3.34 km/h.

SAR DPCA detection

As previously discussed, SAR ATI and SAR DPCA analyses should be equally capable of providing target velocity measurements for target speeds significantly greater than the minimum detectable velocity. As DPCA relies on point by point subtraction to null stationary targets, it is more sensitive to channel gain imbalance. Both approaches are equally sensitive to local variations in scene coherence.

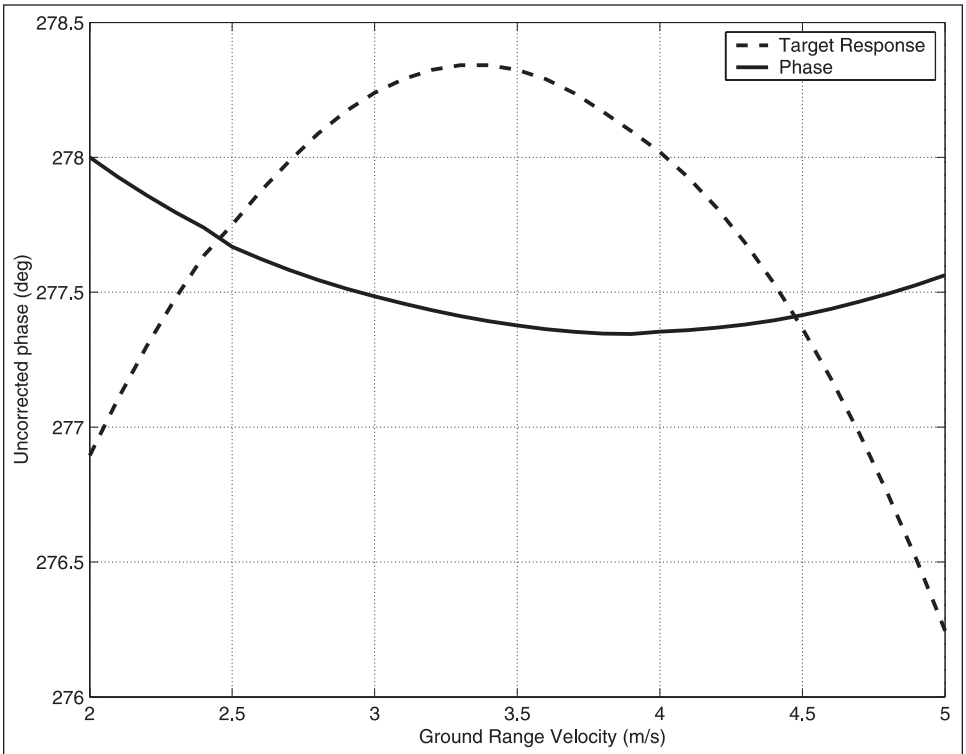

Figure 14. Phase and response versus ground range velocity offset. Response (broken line) not to scale; phase (solid line) to scale. Messer Road target from line 7, pass 10.

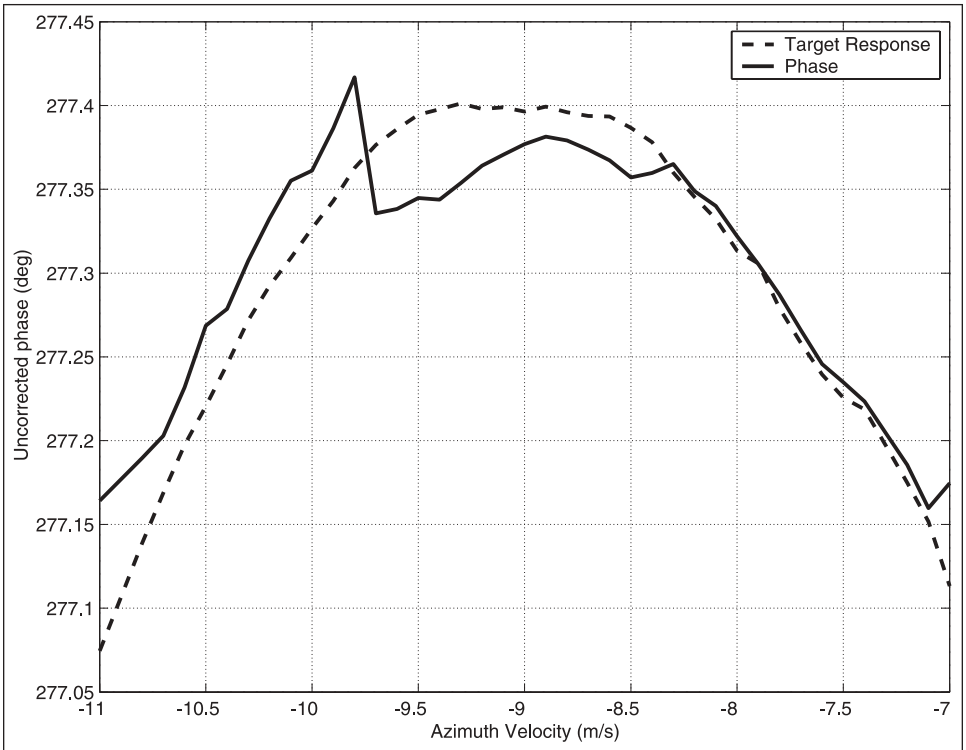

Figure 15. Phase and response versus azimuth velocity offset. Response (broken line) not to scale; phase (solid line) to scale. Messer Road target from line 7, pass 10.

Targets were detected by passing the minimized residual through a magnitude threshold filter. The Stewart Road target had to be processed using velocity offsets (see previous section) due to its high radial velocity. The radial velocity was

Table 3. Ground mover velocity estimates and associated relative and absolute error from the 1999 Petawawa experiment using velocity-adapted SAR (VASAR) processing and ATI.

Pass No.	Target	ATI phase (radians)	Radial velocity (m/s)	Predicted velocity (km/h)	Measured velocity (km/h)	Relative error (%)	Absolute error (km/h)
7	Delta	0.6278	1.539	9.04	9.17	1.42	0.13
7	Juliet	1.4518	3.550	21.45	21.50	0.23	0.05
7	Messer	–1.4135	–3.457	–37.68	–37.12	1.51	0.56
7	Stewart	–3.4632	–8.470	–56.04	–68.20	17.83	12.16
8	Delta	–0.7606	–1.901	–9.51	–9.90	3.94	0.39
8	Juliet	–1.5248	–3.816	–22.26	–24.34	8.55	2.08
8	Messer	–1.0507	–2.630	–36.05	–38.18	5.58	2.13
8	Stewart	–3.5945	–8.995	–69.88	–69.13	1.08	0.75
9	Delta	1.2070	3.052	17.64	20.50	13.95	2.86
9	Juliet	2.1623	5.476	32.65	32.03	1.94	0.62
9	Messer	–1.9761	–5.004	–54.79	–52.03	5.30	2.76
9	Stewart	–2.9302	–7.417	–47.60	–46.45	2.48	1.15
10	Delta	–1.6419	–4.250	–21.15	–21.00	0.71	0.15
10	Juliet	–2.2471	–5.817	–34.00	–32.45	4.78	1.55
10	Messer	–1.4066	–3.644	–55.03	–53.31	3.23	1.72
10	Stewart	–2.5232	–6.521	–50.43	–49.24	2.42	1.19

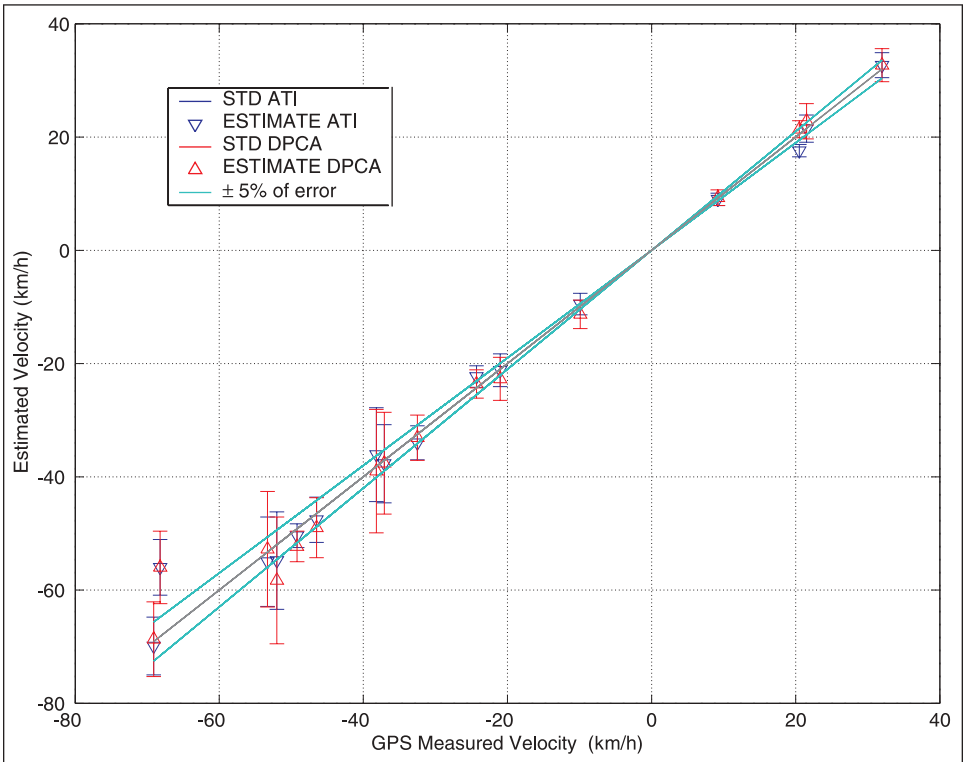

Figure 16. SAR ATI and SAR DPCA measurements of controlled moving target speeds compared with GPS-measured target speeds (Petawawa 1999). Blue lines represent the 5% speed error envelope. The standard deviations are computed from the spread of the sample points that represent a single target in the SAR–GMTI measurements.

estimated from the peak target response in scenes $\{S_1\}$ and $\{S_2\}$ using

$$s_{\text{targ}} = \pm \sin^{-1}\left(\frac{|S_1 - S_2|}{|S_1| + |S_2|}\right)\frac{\lambda}{2\pi\tau} \tag{17}$$

Table 4. Ground mover velocity estimates and associated relative and absolute error from the 1999 Petawawa experiment using VASAR processing and DPCA.

Pass No.	Target	Radial velocity (m/s)	Predicted velocity (km/h)	Measured velocity (km/h)	Relative error (%)	Absolute error (km/h)
7	Delta	1.589	9.33	9.17	1.77	0.16
7	Juliet	3.780	22.84	21.50	6.22	1.34
7	Messer	–3.453	–37.63	–37.12	1.39	0.51
7	Stewart	–8.464	–56.00	–68.20	17.89	12.20
8	Delta	–2.256	–11.29	–9.90	14.01	1.39
8	Juliet	–4.049	–23.62	–24.34	2.95	0.72
8	Messer	–2.849	–39.05	–38.18	2.27	0.87
8	Stewart	–8.839	–69.33	–69.13	0.29	0.20
9	Delta	3.694	21.35	20.50	4.15	0.85
9	Juliet	5.486	32.71	32.03	2.13	0.68
9	Messer	–5.325	–58.30	–52.03	12.06	6.27
9	Stewart	–7.637	–49.01	–46.45	5.52	2.56
10	Delta	–4.568	–22.73	–21.00	8.26	1.73
10	Juliet	–5.662	–33.10	–32.45	1.99	0.65
10	Messer	–3.499	–52.84	–53.31	0.88	0.47
10	Stewart	–6.760	–52.28	–49.24	6.17	3.04

Four out of five GMTs were consistently detected by SAR DPCA for all four radar passes, but the MIT could not be reliably extracted from the residual stationary-world cluster. **Table 4** summarizes the SAR DPCA results in comparison with the GPS-measured speeds. A graphical representation in **Figure 16** allows direct comparison between SAR DPCA and SAR ATI measurements for the controlled moving targets.

The absolute error of DPCA target velocity estimate has an RMS value of 3.66 km/h, which is only slightly higher than the error of 3.34 km/h for ATI. The similarity between DPCA and ATI measurements shows that both methods have similar error ranges, though either may be more advantageous in certain applications.

Targets of opportunity

When the SAR image shown in **Figure 8** is examined in detail in the vicinity of the monitored section of Highway 17, no vehicle returns are seen on or near the road. The application of either ATI or DPCA algorithms to data processed under the stationary-world assumption does not reveal fast moving vehicle returns. A closer examination of the data set is shown in **Figure 17**. In this case, slow-moving control targets are visible, but no other movers are seen.

From video monitoring of this segment of road, the highway was busy throughout the observation period. Application of VASAR processing to the line 7, pass 10 data set (**Figure 17**) was followed by ATI filtering and target extraction to create a moving-target image plane. This was superimposed on the "stationary-world" ATI image to create the SAR components of **Figure 18**. The previously discussed matched-filter optimization procedure was applied to a transport truck travelling southeast at approximately 100 km/h. The cluster of vehicles near the truck was travelling in the same direction, with individual vehicles moving at similar speeds. The two vehicles at the front of the cluster were moving between 10 and 30 km/h faster than the rest, and the third vehicle to the right of the transport was moving 10 km/h slower than the truck. Vehicle speed measurements from the radar (100 ± 5 km/h for the transport) are supported by speed estimates from the video camera system (104 ± 4 km/h). Speed estimates made from video recordings of the highway lie between 98 and 104 km/h for the majority of the vehicles. The slowest vehicle speed was measured at 95 km/h and the fastest at 134 km/h.

The vehicle images in **Figure 18** were extracted from the video records at the times corresponding to the target positions in the ATI image.

Summary and conclusions

The data acquired in this experiment support both SAR ATI and SAR DPCA methods of isolating moving objects in the imaged scene and measuring their velocities. Both approaches yield complex image planes in which the target phase angle (ATI) or magnitude (DPCA) is a direct measure of scene radial velocity.

SAR ATI signal space histograms were tested against a complex PDF derived for jointly Gaussian, correlated radar scenes. The marginal amplitude distributions predicted by the model are not in good agreement with the data, but the marginal phase distribution provides a very robust description (for the terrain observed in the experiment) of the ATI "stationary-world" phase. The marginal phase PDF adapts to vegetation internal-motion effects through local measures of scene coherence. Examination of the RMS phase–amplitude relationship for two uniform, terrain-cover types reveals internal motion characteristics that are in rough agreement with an internal motion, power-law model.

A "keyhole" filter, based on the marginal phase distribution, was used to partition the ATI data into "stationary" data points (those between the filter threshold and the real axis) and moving points (all of those whose phase angle is greater than that defined by the filter threshold). With the exception of the small corner reflector at low speed (20 m^2 RCS, 5 km/h) mounted on the MIT transporter, all moving targets were automatically partitioned from the ATI clutter data set. Moving target false alarms did not appear at the filter settings used in this experiment. False-alarm rate and target detection limit investigations with this data set will be the topic of another paper.

Stationary scene elements in the SAR DPCA signal space form a symmetric distribution about the origin of the complex plane (uniform phase distribution). Near the origin the DPCA distribution is dominated by a mixture of additive noise, almost cancelled (nearly coherent) scene differences, and phase noise modulated scene elements. At larger amplitudes, including the tail of the distribution, scene elements modulated by phase noise and internal motion effects are most significant. The SAR DPCA probability density function was not studied in this paper.

The moving-target results presented in this paper were extracted from the DPCA data by retaining only those image elements with amplitudes larger than an arbitrarily selected threshold that yielded no false alarms in a forest region known to contain no movers. All targets except the MIT were detected and analysed.

SAR imagery is normally formed under the assumption that the measured scene is stationary. Matched filters used for image formation are normally designed to compensate for only the relative motion between the radar system and the Earth. When scene elements move sufficiently fast with respect to the Earth, their radar returns are mismatched with respect to the processing filter, and these elements are defocused, attenuated, and displaced in the azimuth direction. When the mismatch between the target signal and the filter is severe, the target is not detectable in the SAR image. For the data processing used in this experiment, a matched filter was designed to accommodate three-dimensional, linear target velocity and linear acceleration. To extract and measure target speeds, this filter was iterated with different linear velocity assumptions on a portion of the data where uncontrolled moving targets were expected. An algorithm based on successive target amplitudes was used to estimate the best radial and azimuthal speeds. These estimates, projected onto the ground surface, were compared with video recording system measurements. The results confirmed that vehicle speeds could be measured to within 5% accuracy. When the correct target speed was inserted into the matched filter, the extracted targets were correctly positioned in the ATI image plane and could be superimposed on the stationary-world image as is shown in **Figure 18**.

In the controlled moving-target component of this experiment, GPS-monitored, moving corner reflectors whose speeds varied from 5.8 to 31.7 km/h were automatically extracted, reprocessed with corrected radial velocity, and measured. Both SAR ATI and SAR DPCA approaches were applied and yielded correct velocities to within 5% error. The

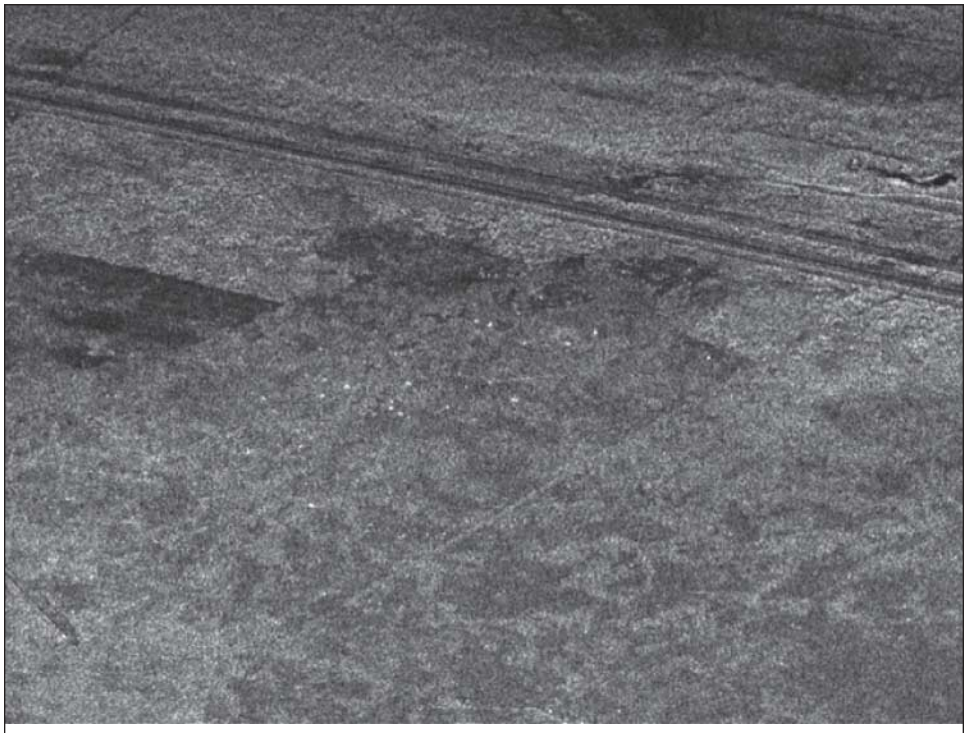

Figure 17. Stationary-world processed ATI image showing Highway 17. No highway traffic is seen.

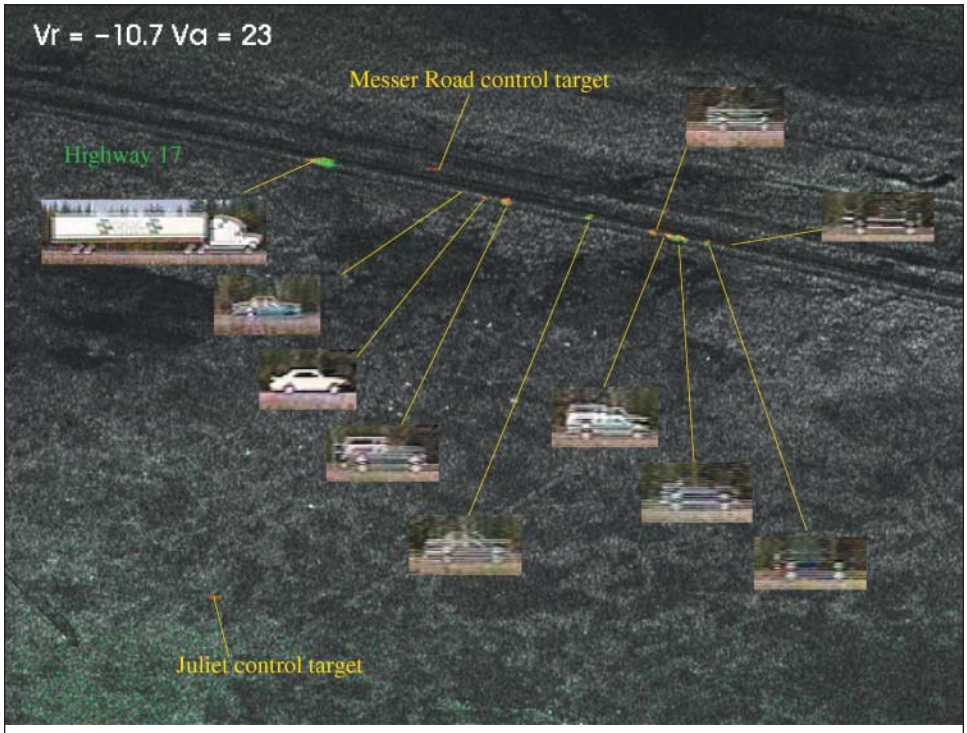

Figure 18. VASAR–ATI-processed vehicles superimposed on **Figure 17**. Vehicle images were extracted from the video monitor. Azimuth velocity (Va) and ground range velocity (Vr) offsets used in SAR matched filter.

errors in the GPS velocity reference measurements are included in the 5% error estimate.

Work with this data set is proceeding to further explore the statistical properties of the ATI and DPCA data sets and to investigate the GMTI detection limits.

RADARSAT-2, like the aircraft used in this experiment, is a two-aperture SAR interferometer, works at a very similar radar frequency, and has the same radar resolution. When used for GMTI measurements, RADARSAT-2 will use beams in the 40–50° incidence-angle range to maximize the radial velocity component of vehicle motion. The airborne experiment reported here was designed to replicate the RADARSAT-2 GMTI mode resolution and observation geometry as closely as possible and to test data-processing algorithms that will be migrated to the RADARSAT-2 GMTI processor. **Table 5** shows the relationship between RADARSAT-2 and the airborne radar used in this experiment.

Although the two radars are very different, the critical SAT–GMTI parameters DPCA registration time, synthetic aperture time, and predicted minimum detectable velocity (MDV) are sufficiently close that results from the airborne experiment can be applied to the space-based radar using signal-simulation techniques. This has been done and is reported elsewhere (Chiu, 2000; Chiu et al., 2000; Chiu and Livingstone, 2002). Simulation studies for RADARSAT-2 have shown that ATI and DPCA target extraction processes are equivalent except for small, slow-moving targets, for which ATI is marginally better. Because of the higher phase noise of the satellite radar, the RADARSAT-2 MDV (15 km/h) is larger than that observed in the airborne experiments (6 km/h); however, the target detection and extraction algorithms tested in the airborne experiment are transferable to the RADARSAT-2 case with few modifications. The phase probability density function theoretically developed for jointly Gaussian scenes has been shown by experiment to be quite robust to clutter heterogeneity and is directly applicable to the design of RADARSAT-2 moving target extraction algorithms. The greatest difference between the airborne and space-based SAR–GMTI capabilities arises from the relationship between the platform velocity and the along-track velocities of moving targets. In the airborne case, the target speeds are a significant fraction of the radar speed, and reasonably accurate azimuthal target speed estimates can be made. This is not true for space-based radars. For the same reason, the RADARSAT-2 target focus will be

Table 5. RADARSAT-2 GMTI mode and CV 580 SAR–ATI mode comparison.

Parameter	RADARSAT-2 mode	CV 580 SAR–ATI mode
Wavelength (m)	0.0555	0.0567
Aperture spacing (m)	7.50	0.27
Platform speed (m/s)	7500	157
Altitude (km)	795	7
DPCA registration time (ms)	1.0	1.7
Synthetic aperture time (s)	0.4	3.3
RMS phase noise (°)	~10	2
MDV (40 m^2 target) (km/h)	15	6

much less sensitive to target motion than the airborne case. The ATI directional ambiguity will occur at 16.7 m/s radial target velocity (78 km/h ground speed at 50°) for the airborne case and at 27.8 m/s radial target velocity (131 km/h ground speed at 50°) for RADARSAT-2. The measurement of radial target velocities follows the same principles for both the airborne and space-based radar cases, and RADARSAT-2 is expected to support target speed measurement accuracies in the 5–10% range.

Acknowledgements

The work presented here was supported by the Canadian Department of National Defence RADARSAT-2 GMTI demonstration project. The authors are grateful for the practical support provided by the pilots and crew of the Environment Canada CV 580 SAR aircraft, the Lockheed Martin training-target support team at Canadian Forces Base Petawawa, the CCRS for stripping the airborne radar data to computer-readable format, and the Commanding Officer and staff of CFB Petawawa. The video images used to validate the target of opportunity measurements were obtained by Janice Lang and Bob Gervais of the Defence Research Establishment Ottawa (DREO) technical services group.

References

Barbarossa, S. 1992. Detection and imaging of moving objects with SAR — Part 1: Optimal detection and parameter estimation. *IEE Proceedings*, Part F, Vol. 138, No. 2, pp. 79–87.

Chiu, S. 2000. *An analysis of RADARSAT 2 SAR-GMTI performance for standard beam mode*. Defence Research Establishment Ottawa (DREO), Technical Report TR 2000-088.

Chiu, S., and Livingstone, C. 2002. Spaceborne GMTI processor development for Canada's Radarsat-2 satellite. In *Use of Space Systems in Integrated Military Missions, Proceedings of the NATO Research and Technology Organisation (RTO) Systems Concepts and Integration Panel (SCI) Symposium*, Lisbon, Portugal, 21–23 May 2001, RTO-MP-080, Vol. 5, pp. 1–17.

Chiu, S., Livingstone, C., Knight, T., and Sikaneta, I. 2000. Computer simulations of Canada's Radarsat-2 GMTI. In *Space Based Observation Technology, Proceedings of the NATO Research and Technology Organisation (RTO) Sensors and Electronic Technology Panel (SET) Symposium*, Samos, Greece, 16–18 October 2000, RTO-MP-61, Vol. 45, pp. 1–8.

Ender, J.H.G. 1996. Detection and estimation of moving target signals by multi-channel SAR. *International Journal of Electronics and Communications (AEU)*, Vol. 50, No. 2, pp. 150–156.

Ender, J.H.G. 1999. Space–time processing for multi-channel synthetic aperture radar. *Electronics and Communication Engineering Journal*, Vol. 1, No. 1, pp. 29–38.

Fitch, J.P. 1991. The single antenna interferometer. In *ICASSP'91, Proceedings of the IEEE International Conference on Acoustics, Speech, and Signal Processing*, Toronto, Ont., 14–17 May 1991, pp. 2573–2576.

Franceschetti, G., and Lanari, R. 1999. *Synthetic aperture RADAR processing*. CRC Press, Boca Raton, Fla. ISBN 0-8493-7899-0.

Freeman, A. 1984. Simple MTI using synthetic aperture radar. In *IGARSS'84, Proceedings of the International Geoscience and Remote Sensing Symposium*, Paris. European Space Agency (ESA), SP-215.

Gierull, C. 2001. *Statistics of SAR interferograms with application to moving target detection*. Defence Research Establishment Ottawa (DREO), Technical Report TR 2001-045.

Joughin, I.R., Winebrenner, D.P., and Percival, D.B. 1994. Probability density functions for multi-look polarimetric signatures. *IEEE Transactions on Geoscience and Remote Sensing*, Vol. 32, No. 3, pp. 562–574.

Just, D., and Bamler, R. 1994. Phase statistics of interferograms with applications to synthetic aperture radar. *Applied Optics*, Vol. 33, No. 20, pp. 4361–4367.

Lee, J.-S., Hoppel, K.W., Mango, S.A., and Miller, A.R. 1994. Intensity and phase statistics of multi-look polarimetric and interferometric SAR imagery. *IEEE Transactions on Geoscience and Remote Sensing*, Vol. 32, No. 5, pp. 1017–1028.

Livingstone, C.E., Gray, A.L., Hawkins, R.K., Vachon, P.W., Lukowski, T.I., and Lalonde, M. 1995. The CCRS airborne SAR systems: radar for remote sensing research. *Canadian Journal of Remote Sensing*, Vol. 21, No. 4, pp. 468–491.

Meisl, P., Thompson, A.A., and Luscombe, A.P. 2000. RADARSAT-2 mission: overview and development status. In *EUSAR 2000, Proceedings of the 3rd European Conference on Synthetic Aperture Radar*, Munich, 23–25 May 2000.

Nathanson, F.E. 1969. *Radar design principles*. McGraw-Hill, New York.

Novak, L.M., Sechtin, M.B., and Cardullo, M.J. 1989. Studies on target detection algorithms that use polarimetric radar data. *IEEE Transactions on Aerospace and Electronic Systems*, Vol. 25, No. 2, pp. 150–165.

Raney, R.K. 1971. Synthetic aperture imaging radar and moving targets. *IEEE Transactions on Aerospace and Electronic Systems*, Vol. 7, No. 3, pp. 499–505.

Sikaneta, I. 2001. *The Convair 580 along-track Insar processor.* Defence Research Establishment Ottawa (DREO), Technical Memorandum TM 2001-053.

Thompson, A.A., and Livingstone, C.E. 2000. Moving target performance for RADARSAT-2. In *IGARSS'2000, Proceedings of the International Geoscience and Remote Sensing Symposium*, Honolulu, Hawaii, 24–28 July 2000.

Touzi, R., and Lopes, A. 1996. Statistics of the Stokes parameters and of the complex coherence parameters in one-look and multi-look speckle fields. *IEEE Transactions on Geoscience and Remote Sensing*, Vol. 34, No. 2, pp. 519–531.

Touzi, R., Lopes, A., Bruniquel, J., and Vachon, P.W. 1999. Coherence estimation for SAR imagery. *IEEE Transactions on Geoscience and Remote Sensing*, Vol. 37, No. 1, pp. 135–149

Yueh, S.H., and Kong, J.A. 1989. K-distribution and polarimetric terrain clutter. *Journal of Electromagnetic Waves and Applications*, Vol. 3, No. 8, pp. 747–768.